Spatial geometric constraints histogram descriptors based on curvature mesh graph for 3D pollen particles recognition*

Xie Yong-Hua(谢永华)[a)†], Xu Zhao-Fei(徐赵飞)[a)], and Hans Burkhardt[b)]

[a)] School of Computer and Software, Nanjing University of Information Science and Technology, Nanjing 210044, China
[b)] Department of Computer Science, Freiburg University, Freiburg 79100, Germany

(Received 21 August 2013; revised manuscript received 25 November 2013; published online 10 April 2014)

This paper presents one novel spatial geometric constraints histogram descriptors (SGCHD) based on curvature mesh graph for automatic three-dimensional (3D) pollen particles recognition. In order to reduce high dimensionality and noise disturbance arising from the abnormal record approach under microscopy, the separated surface curvature voxels are extracted as primitive features to represent the original 3D pollen particles, which can also greatly reduce the computation time for later feature extraction process. Due to the good invariance to pollen rotation and scaling transformation, the spatial geometric constraints vectors are calculated to describe the spatial position correlations of the curvature voxels on the 3D curvature mesh graph. For exact similarity evaluation purpose, the bidirectional histogram algorithm is applied to the spatial geometric constraints vectors to obtain the statistical histogram descriptors with fixed dimensionality, which is invariant to the number and the starting position of the curvature voxels. Our experimental results compared with the traditional methods validate the argument that the presented descriptors are invariant to different pollen particles geometric transformations (such as posing change and spatial rotation), and high recognition precision and speed can be obtained simultaneously.

Keywords: pollen recognition, curvature mesh graph, spatial geometric constraints, bidirectional histogram

PACS: 07.05.Tp, 42.30.Wb **DOI:** 10.1088/1674-1056/23/6/060701

1. Introduction

The classification of biological particles is one of the most important techniques in a wide range of applications, such as cell classification for auxiliary diagnosis, paleoclimatic reconstruction, derivation of geographical origin of products, study of allergenic processes in medicine, index forecasting for people with pollen hypersensitivity, etc. The principal tasks in almost all of these applications are to classify and count biological particles, which should be done manually by highly skilled experts under microscopy.[1,2] A high level of training is needed to obtain accurate identification results, and the commonly used discrimination criterion is the visual morphological appearance of biological particles, such as shape, polarity, aperture, size, exine stratification and thickness, and so on.[3] This work is laborious and time consuming, and always brings about some wrong identifications. Automated pollen particle classification and recognition is no exception and has been greatly focused on in recent years.[4,5] Due to the fact that different categories of pollen particles can be represented effectively through some intrinsic digitalized image features, such as morphology, texture, shape, geometric and statistical features, etc., using the technologies of computer vision and pattern recognition for automated pollen image classification has become an innovative approach to the cross-disciplinary research of computer vision, biology, and environmental protection.[6,7] Since most pollen images are usually recorded as a full 3D volumetric data set with confocal laser scanning microscopy, any two-dimensional (2D) representation of these 3D pollen structures usually involves a substantial loss of information. A clear tendency appears towards the study of cells and cell clusters including whole organisms in their natural 3D environment.[2,8] In recent years, a number of descriptors have been developed for characterizing the 3D volumetric pollen particles, which can be classified into two groups: integral invariant descriptors and structural descriptors. The integral invariant descriptors, such as the MiSP descriptors,[9] the GSGI descriptors,[10] and the BGPK descriptors,[11] can effectively describe the statistical voxels distribution of the 3D pollen particles and have been proved to be invariant to the rotation and translation of pollen images. However, through the abnormal acquisition approach, most 3D pollen images are usually recorded with high dimensionality and redundant information, as well as noise disturbance caused by pollen pollution. Since the integral invariant descriptors are directly computed by taking all of the surface voxels of the pollen images as primitive discriminant features, the computation cost is very high and the recognition rate on the degraded pollen images is quite low. As for the structural descriptors, some vector-based primitive information, such as dominant points, contours, lines, and arcs, is first

*Project supported by the National Natural Science Foundation of China (Grant No. 61375030), the Natural Science Foundation of Jiangsu Province, China (Grant No. BK20090149), and the Natural Science Foundation of Higher Education Institutions of Jiangsu Province, China (Grant No. 08KJD520019).

†Corresponding author. E-mail: yonghua@nuist.edu.cn

© 2014 Chinese Physical Society and IOP Publishing Ltd

extracted to characterize the original pollen images prior to feature extraction. The representative structural descriptors include the invariant moment descriptors,[12] such as the subset Zernike moment descriptors (SZMD),[13] the deformable template matching descriptors (DTMD),[14] the statistical matrix curvature descriptors (SMCD),[15] and the visual shape context descriptors (VSCD).[16] Although the dimensionality can be greatly reduced using these methods, the noise disturbance of the degraded pollen images can result in the changes of the vector-based primitive pollen information. Such changes will make the subsequent extracted descriptors unstable. Furthermore, it is also very difficult to normalize the fixed size and the starting point of the traditional structural descriptors for exact similarity evaluation.

In order to extract highly compact and invariant descriptors for the pollen images with different qualities, we take both voxel-unrelated structural information and statistical algorithm into consideration, and then present the spatial geometric constraints histogram descriptors (SGCHD) based on curvature mesh graph for the 3D pollen recognition. In this method, surface curvature voxels are first extracted as the primitive information of the original pollen images, to effectively reduce the high dimensionality and eliminate the noise disturbance in the original pollen images. Bidirectional histogram algorithm is then applied to the spatial geometric constraints vectors to obtain the statistical histogram descriptors with fixed dimension. Experimental results on the two standard pollen image databases show that high recognition accuracy and speed can be obtained simultaneously with the proposed descriptors.

The rest of this paper is organized as follows. In Section 2, the construction of the curvature mesh graph is introduced. The computation of the spatial geometric constraints is also presented in this section. In Section 3, we present the steps for constructing the normalized geometric constraints histogram descriptors. The experimental results and conclusion are presented in Section 4 and Section 5, respectively.

2. Curvature mesh graph and spatial geometric constraints

2.1. Curvature mesh graph

On account of the fact that 3D pollen images usually have a huge amount of surface information as well as the noise disturbance caused by the microscopy sensors and the irregular collection process, it is desirable to have a more compact intermediate representation of 3D pollen images for the purpose of reducing the redundant information and different disturbances. Surface curvature has been used extensively in the literature for mesh simplification and smoothing, object recognition, and mesh segmentation in 3D spatial coordinates. The corresponding curvedness measures the intensity of the surface curvature and describes how gently or strongly curved a surface is. The surface curvature voxels actually are the rigid feature points with the local curvature information at multiple scales, which can retain the principal structural information about surface curvedness and reduce the noise and deformation disturbance effectively.[17,18] With a given threshold, the surface curvature voxels corresponding to the principal curvedness are selected as suitable primitive points for representing the intrinsic pollen volumetric data. Mathematically, this can be defined as follows.

Let $z = f(x,y)$ be the function of the 3D image surface S in 3D rectangular coordinates. Let t_{p_i} be a tangent vector on the surface at the point $p_i \in S$ with $\|t_{p_i}\| = 1$, the normal curvature of S in the direction of t_{p_i} is defined as

$$C(t_{p_i}) = T(t_{p_i})t_{p_i}, \tag{1}$$

where $i \in [1,M]$, M is the total number of the pixels on the surface S, $T(t_{p_i}) = -D(t_{p_i})U$ is the shape operator with U being the field of surface normal vectors defined in a neighborhood of p, $D(t_{p_i})U$ denotes the derivative of U with respect to t_{p_i}.

To the normal curvature $C(t_{p_i})$, the maximum and minimum principle curvatures, $C_{\max}(p_i)$ and $C_{\min}(p_i)$, respectively, can be obtained as the principal curvatures at the point $p_i \in S$, which can be defined as

$$C_{\max}(p_i) = H(p_i) + \sqrt{H^2(p_i) - K(p_i)}, \tag{2}$$

$$C_{\min}(p_i) = H(p_i) - \sqrt{H^2(p_i) - K(p_i)}, \tag{3}$$

where $H(p_i)$ and $K(p_i)$ denote the mean curvature and the Gaussian curvature at the point $p_i \in S$, respectively.

Then, the bending energy of the surface named curvedness at the point $p_i \in S$ is obtained as

$$C(p_i) = \sqrt{(C^2_{\max}(p_i) + C^2_{\min}(p_i))/2}. \tag{4}$$

The curvedness is used to indicate how strongly or gently curved a surface is. When the curvedness at a given point approaches zero, the surface patch around this point will gradually become planar. The curvedness will be zero for those completely planar surface patches. Therefore, the higher curvedness actually reflects the sharp bending degree of surface patches, which can effectively describe the primary local surface features. In order to reduce a large amount of redundant information, a threshold is used to choose the principal surface points with the predominant curvedness as the curvature voxels for subsequent feature extraction, which can be described as follows.

Let $\{p_1, p_2, \ldots, p_i \ldots, p_M | p_i(x_i, y_i, z_i) \in R^3\}$ be the collection of all the voxles on the 3D volumetric image surface S, then the mean of the curvedness for all the voxels will be computed as

$$\overline{C_p} = \frac{1}{M}\sum_{i=1}^{M} C_{p_i}. \tag{5}$$

Taking the curvedness mean as the threshold, the compressed curvature voxels collection P with the principal curvedness can be selected as the feature points and is given as

$$P = \{p_j | C_{p_j} \geq \overline{C}; j \in [1, N]\}, \tag{6}$$

where N is the number of the selected curvature voxels in the collection P and satisfies the constraints $N \leq M$. Figure 1 presents two examples of curvature voxles extraction for the same pollen recorded by two different microscopes.

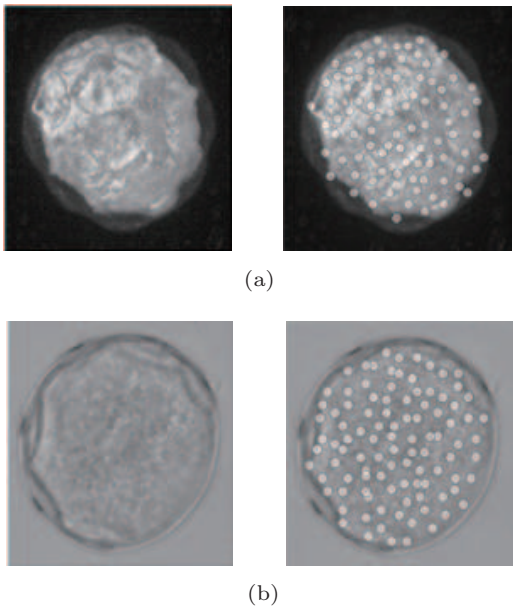


Fig. 1. Curvature voxels extraction for the same category of pollen (a) confocal pollen and (b) pollenmonitor pollen.

By connecting all of the curvature voxels in the collection P with line segments, the spatial curvature mesh graph is constructed to approximate structure information of the original 3D pollen images. Obviously, the curvature mesh graph only uses some principal voxels instead of all the 3D pollen surface pixels as the feature points for subsequent feature extraction, which can effectively reduce the high dimensionality and noise disturbance of the original 3D pollen images.

2.2. Spatial geometric constraints

Since it is quite difficult to normalize the fixed size and the starting position, the traditional structural voxels cannot be directly used as discriminant features for exact similarity evaluation. We notice that the geometric constraints between each curvature voxel can effectively describe the geometric feature for determining the structure of an image. Consequently, the geometric constraints based on the spatial curvature mesh graph are proposed to characterize the image structure. These steps are described as follows.

First, to the N selected curvature voxels $p_1, p_2, \ldots, p_N$ in the collection P, one part of the curvature mesh graph based on several curvature voxels is presented in Fig. 2(a), in which p_1 is taken as the basic voxel and connects to the other voxels so as to show how all the other curvature voxels distribute surrounding p_1. Meanwhile, considering that the geometric distribution based on the curvature mesh graph can be described as the edge and angle geometric constraints between any two curvature voxels, we randomly select three curvature points p_b, p_u, p_v from the collection P as examples to describe the geometric constraints.

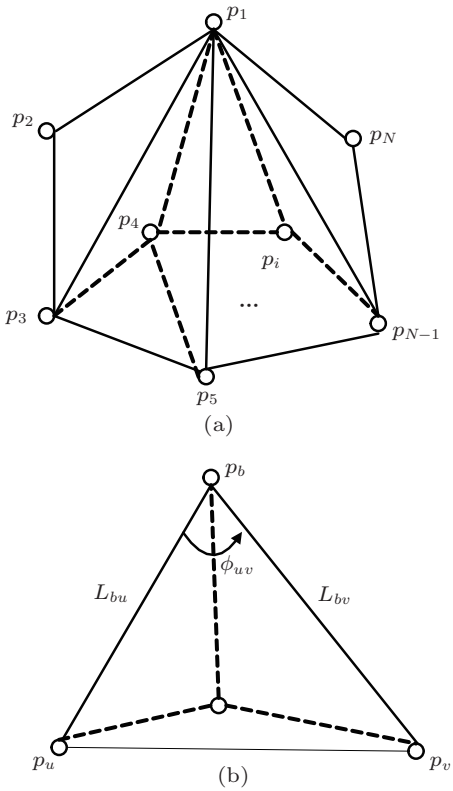


Fig. 2. (a) geometric distribution of curvature points and (b) geometric constraints among three curvature points.

Second, in order to simplify the description of our idea, we only take p_b as the basic voxel, and p_u and p_v as the other two voxels which are constraint to p_b through the spatial geometric relations. As shown in Fig. 2(b), let L_{bu} and L_{bv} denote the distance between p_b and p_u, p_b and p_v, namely the length of the two vectors $p_b p_u$ and $p_b p_v$ separately, and let ϕ_{uv} be the angle between the two vectors, the spatial edge constraints and angle constraints for the basic voxel p_b can be, respectively, defined as

$$D_{uv} = \min(L_{bu}/L_{bv}, L_{bv}/L_{bu}), \tag{7}$$

$$\phi_{uv} = \angle p_u p_b p_v / 360. \tag{8}$$

Then the combined spatial geometric constraints vectors between p_u and p_v for the basic curvature voxel p_b are grouped together and described as $\{D_{uv}, \phi_{uv}\}^{\mathrm{T}}$. It is obvious that the edge constraints D_{uv} and the angle constraints ϕ_{uv} are invariant to image rotation and scaling transformation, and can be used

to effectively describe the structure of the pollen images. Accordingly, the subsequent extracted descriptors based on the two constraints are also geometrically invariant.

Third, since there are N curvature voxels of p_1, p_2, ..., p_N in the collection P, we apply the same steps to each curvature voxel and then obtain $(N-1)(N-2)/2$ spatial edge constraints and angle constraints, which can be described as a two-dimensional vector set $\{(D_{ij},\ \phi_{ij})^{\mathrm{T}} | i \in [2, N-1], j \in [i+1, N]\}$. The edge constraints D_{ij} and the angle constraints ϕ_{ij} for the N curvature voxels are actually two matrixes with the dimensionality of $N \times ((N-1)(N-2)/2)$, where N denotes the number of the compressed curvature voxels in collection P and $(N-1)(N-2)/2$ denotes the dimensionality of the geometric constraints for each curvature voxel.

3. Spatial geometric constraints histogram descriptors

Although effective for describing the structure information of pollen images, the geometric constraints are still inappropriate for exact similarity match due to the high dimensionality and the variable sort order of the curvature voxels. Moreover, the unequal number of curvature voxels may cause the size of the directly extracted constraints vectors for different pollen images to be unequal. Due to the fact that the histogram distribution of the geometric constraints can keep invariant to image rotation, translation, and the sort order of the curvature voxels,[19] we apply the bidirectional histogram algorithm on the geometric constraints matrixes to obtain the statistical descriptors with fixed dimensionality for pollen recognition. Similarly, we only take the edge constraints as an example to explain the extraction steps of the descriptors.

Without loss of generality, the curvature voxel p_1 in the collection P is regarded as the reference voxel. As mentioned above, the edge constraints between the reference voxel p_1 and all the other curvature voxels can be described as $\{D_{ij} | i \in [2, N-1], j \in [i+1, N]\}$. Since D_{ij} has been normalized into the interval $[0, 1]$, we averagely separate $[0, 1]$ into K subset bins with the same size according to the energy distribution of the row edge constraints. Let $n_k(p_1)$ denote the number of the edge constraints located in the k-th subset bin, which can be calculated as

$$n_k(p_1) = \sum_{i=2}^{N-1} \sum_{j=i+1}^{N} r_k(D_{ij}), \tag{9}$$

$$r_k(D_{ij}) = \begin{cases} 1, & D_{ij} \in \text{ the } k\text{-th bin}, \\ 0, & \text{else}. \end{cases} \tag{10}$$

The probability distribution of the edge constraints located in the k-th subset bin for the reference voxel p_1 can be defined as

$$w_k(p_1) = \frac{2}{(N-1)(N-2)} n_k(p_1), \tag{11}$$

where $1 \le k \le K$.

Through applying the above method to each subset bin for the curvature point p_1, the corresponding row edge constraints histogram vector can be obtained as $\{w_1(p_1),\ w_2(p_2),\ \ldots,\ w_k(p_1),\ \ldots,\ w_K(p_1)\}$. Similarly, let each of the curvature voxels in the collection P alternately act as the reference point, the row histogram algorithm is applied to each row vector of the edge constraints matrix consisting of the edge constraints for each curvature voxel, to obtain the row edge constraints histogram matrix W

$$W_{N\times K} = \begin{pmatrix} w_1(p_1) & w_2(p_1) & \ldots & w_K(p_1) \\ w_1(p_2) & w_2(p_2) & \ldots & w_K(p_2) \\ \vdots & \vdots & \ddots & \vdots \\ w_1(p_N) & w_2(p_N) & \ldots & w_K(p_N) \end{pmatrix}. \tag{12}$$

In fact, the column vector of the edge histogram matrix describes the edge geometric constraints distribution in the same subset bin for each curvature voxel. In order to make the matrix column vector invariant to the number of the curvature voxels for different pollen images, we continue to apply the column histogram method to each column vector of the row edge constraints histogram matrix W. Similarly, the interval $[0, 1]$ is averagely divided into L subset bins. For the vector of column k, the probability of the elements falling into the l-th subset bin can be defined as

$$x_l(k) = \frac{1}{N} \sum_{r=1}^{N} u_l(w_k(p_r)), \tag{13}$$

$$u_l(w_k(p_r)) = \begin{cases} 1, & w_k(p_r) \in \text{ the } l\text{-th bin}, \\ 0, & \text{else}, \end{cases} \tag{14}$$

where $1 \le k \le K$ and $1 \le l \le L$.

Through the same method, we apply the column histogram method to each column vector of the matrix W to obtain the final edge constraints histogram descriptors

$$X_{L\times K} = \begin{pmatrix} x_1(1) & x_1(2) & \ldots & x_1(K) \\ x_2(1) & x_2(2) & \ldots & x_2(K) \\ \vdots & \vdots & \ddots & \vdots \\ x_L(1) & x_L(2) & \ldots & w_L(K) \end{pmatrix}. \tag{15}$$

Due to the fact that the angle constraints for each curvature point have also been normalized into the interval $[0, 1]$, the angle constraints histogram descriptors with respect to the matrix θ_{ij} can be extracted with the same bidirectional histogram method. After the interval $[0, 1]$ in the row and column directions for the angle constraints matrix $\{\phi_{ij} | i \in [2, N-1], j \in [i+1, N]\}$ have been divided into Q and R subset bins, the angle constraints histogram descriptors can be obtained as

$$Y_{R\times Q} = \begin{pmatrix} y_1(1) & y_1(2) & \ldots & y_1(Q) \\ y_2(1) & y_2(2) & \ldots & y_2(Q) \\ \vdots & \vdots & \ddots & \vdots \\ y_R(1) & y_R(2) & \ldots & y_R(Q) \end{pmatrix}. \tag{16}$$

In order to effectively characterize the overall statistical distribution of the geometric constraints for each curvature voxel, the edge and angle histogram descriptors are grouped together to form the final SGCHD features, which can be described as $\{X,Y\}^{\mathrm{T}}$. Obviously, the histogram feature usually represents the energy distribution of the original geometric constraints in different subset bins, which are invariant to the curvature itself and the number of curvature voxels. The SGCHD features based on it can keep the spatial geometric structure for a 3D model, which are invariant to image rotation, translation, and the sort order of the curvature voxels.

4. Experimental results

Experiments are performed on two standard pollen image datasets with a Pentium IV computer of 2.8-GHz CPU and 6-GB memory. The confocal dataset is the laboratory pollen image dataset with 389 pollen grains of 26 different categories, in which the images were directly from the plants and manually recorded as a full 3D volumetric data set with the confocal laser scanning microscopy. All of the confocal pollen images have high quality without any deformation and contamination. Pollenmonitor dataset is a real-world dataset with 22750 pollen grains from 33 categories, in which all the images were automatically collected, prepared and recorded by the first prototype of the pollenmonitor in Europe in 2006.[20] Some images in this dataset are of low quality of deformation and contamination caused by the microscopy sensors and the irregular collection method in the real collection process. Meanwhile, all of the images in the two datasets take on respective appearance of different geometric transformations, such as pose change, spatial rotation, and so on. In order to validate the good geometric invariance of our proposed SGCHD, the images were not geometrically normalized before the feature extraction. The number of curvature voxels varies greatly between the Confocal pollen images and Pollenmonitor pollen images due to the different original image sizes, which are 3000 and 21320, respectively. For the purpose of keeping enough local discriminant features and reducing computation complexity simultaneously, the number of subset bins in the row and column direction of geometric constraints histogram matrix are set as 20 and 15 for Confocal pollen images, and 52 and 41 for Pollenmonitor pollen images, which are constrained to the pollen image resolution. The dimensionality of final edge and angle histogram matrix for the two pollen images can be reduced to 300 and 2132, respectively. The experiments were performed by taking 20% of the images of each category as training images and the remaining ones as test images with random selection. A minimum distance classifier is used for the final feature classification. Let $\{X_i,Y_i\}$ and $\{X_j,Y_j\}$ denote the SGCHD extracted from any two pollen images, the distance between them can be defined as

$$d_{ij} = (d_{\min}(X_i,X_j) + d_{\min}(Y_i,Y_j))/2, \tag{17}$$

where the function $d_{\min}(\,)$ denotes the minimum distance classifier.

The performance index of correct recognition rate (CRR), rejected rate (RR), false recognition rate (FRR), and recognition time (RT) are used to evaluate the recognition performance of the descriptors. The chart of average recognition precision versus average recall rate is used to demonstrate the relations among the number of correct recognition examples, the false recognition examples, and the rejected examples. Furthermore, in order to validate the performance of our proposed descriptors, the average recognition results of the SGCHD are also compared with those of the four traditional descriptors on two pollen image datasets, which include the subset Zernike moment descriptors (SZMD),[13] the deformable template matching descriptors (DTMD),[14] the statistical matrix curvature descriptors (SMCD),[15] and the visual shape context descriptors (VSCD).[16]

4.1. Results of the confocal dataset

Figure 3 presents the recognition results based on six representative pollen categories from the Confocal dataset. It is shown that, without deformation and contamination, most of the confocal pollen images that have a clear edge and abundant local structure information have been correctly classified. The experimental results validate that the proposed SGCHD can keep good invariance to the geometric transformation of pose change and spatial rotation for the Confocal dataset pollen images. The detailed experimental results are presented in Table 1. It can be inferred that the recognition performance for different pollen categories varies greatly, which is caused by the change of the qualities of the pollen images and the dimensionality of structure information. For example, among all the pollen categories, the Compositae pollen images have the clearest edge and the most abundant local structure information, on which the highest 100% correct recognition rate can be obtained without any rejected and falsely classified examples, while the correct recognition results based on the Acer pollen images can only reach 53.8% together with a corresponding 46.2% rejected and falsely recognition results. The rejected examples and falsely classified examples are mainly caused by the obscure surface structures, which may result in the variation of the extracted curvature voxels and the subsequent extracted SGCHD features.

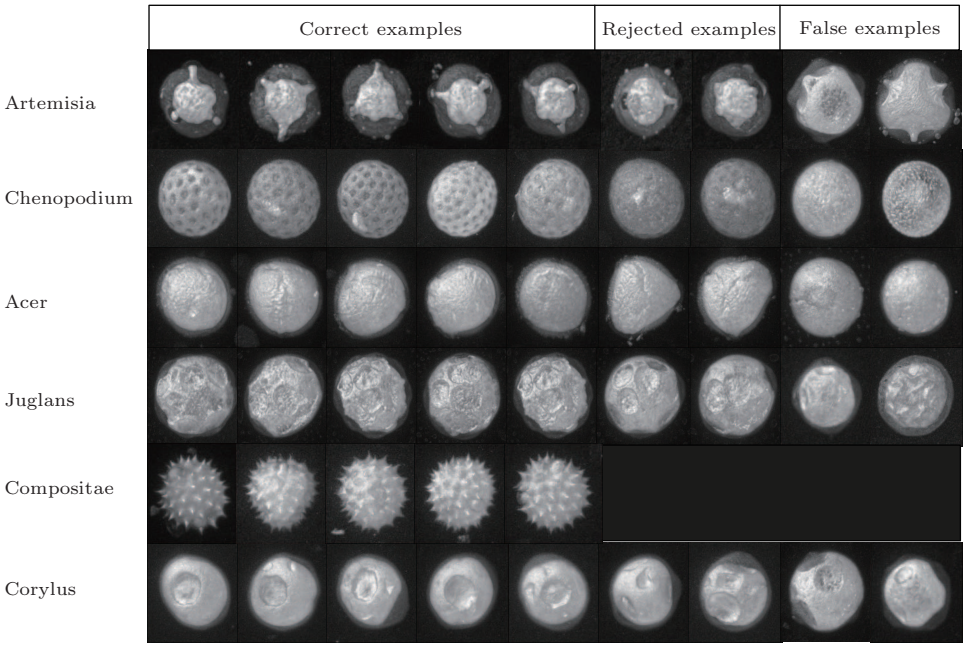


Fig. 3. Top recognition examples on 6 pollen categories from the Confocal dataset.

Table 1. Recognition results on 6 pollen categories from the Confocal dataset.

Pollen category	CRR/%	RR/%	FRR/%
Artemisia	97.2	0	2.8
Chenpodium	91.7	3.2	5.1
Acer	53.8	25.6	20.6
Juglans	92.3	2.8	4.9
Corylus	90.1	4.6	5.3
Compositae	100	0	0

Table 2 presents a comparison of the average recognition results for different methods on the Confocal dataset. The parameters of feature number and recognition time are also presented in this table in order to evaluate the computation complexity of different descriptors. Figure 4 presents the recognition performance of average recall rate versus average recognition precision for all of the pollen categories. It is obvious that the average recognition performance of the SGCHD is far superior to that of the other four traditional descriptors. First, with the SGCHD, the average correct recognition rate of the 26 pollen categories on the Confocal dataset can reach 97.2%, which outperforms that of the other four methods by the 5.5% improvement averagely. The corresponding average rejected rate and false recognition rate can be controlled as 1.3% and 1.5%, respectively. Second, the SGCHD are actually the statistical features extracted based on the compressed curvature voxels and bidirectional histogram algorithms, which can greatly reduce both the redundant information and the high dimensionality of the descriptors for the 3D pollen images. For example, compared with the SZMD and SMCD, the feature number of the SGCHD can be reduced by about 94.7% and 97.8%, respectively. The average recognition time, including the feature extraction time and the classification time, can be calculated as 2.2 s on the Confocal dataset, which is far superior to those of the other traditional descriptors. The experimental results validate that the SGCHD are quite suitable for practical pollen classification because of the low feature dimensionality and good geometric invariance.

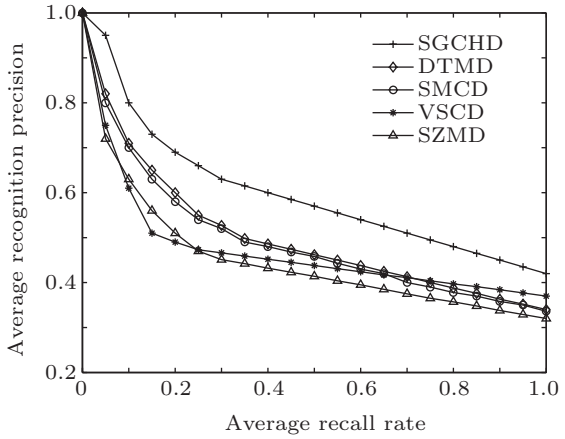


Fig. 4. Average recognition precision versus average recall rate on the Confocal dataset.

Table 2. Contrast recognition results of different descriptors on the Confocal dataset.

Descriptors	FN	CRR/%	RR/%	FRR/%	RT/s
SZMD	5620	88.7	5.6	5.7	15.3
DTMD	3375	93.0	3.4	3.6	16.2
SMCD	13600	92.6	2.9	4.5	8.5
VSCD	680	92.7	2.7	4.6	8.2
SGCHD	300	97.2	1.3	1.5	2.2

4.2. Results of the Pollenmonitor dataset

The top recognition examples from six representative pollen categories from the Pollenmonitor dataset are presented in Fig. 5. It is shown that the pollen images in the same category take on different appearance and structures caused by the different micrographic collection methods. The experimental examples demonstrate that most of the pollens with different pose and spatial rotation can be correctly classified in the Pollenmonitor dataset. Table 3 presents the detailed recognition results on the six pollen categories. It can be seen that the recognition performance also differs from each other due to the variant pollen qualities. The average correct recognition rate reaches 87.2% with the corresponding 3.6% rejected rate and 9.2% false recognition rate, respectively. The highest correct recognition rate of 90.8% is obtained on the classification of the Corylus pollens, while the recognition rate on the Aesculus pollens can only reach 43.2%, with two examples being correctly classified. The rejected examples are mainly those pollen images with low qualities caused by the deformation and contamination during the collection process, which will result in the variance of the curvature voxels and the subsequent extracted histogram descriptors.

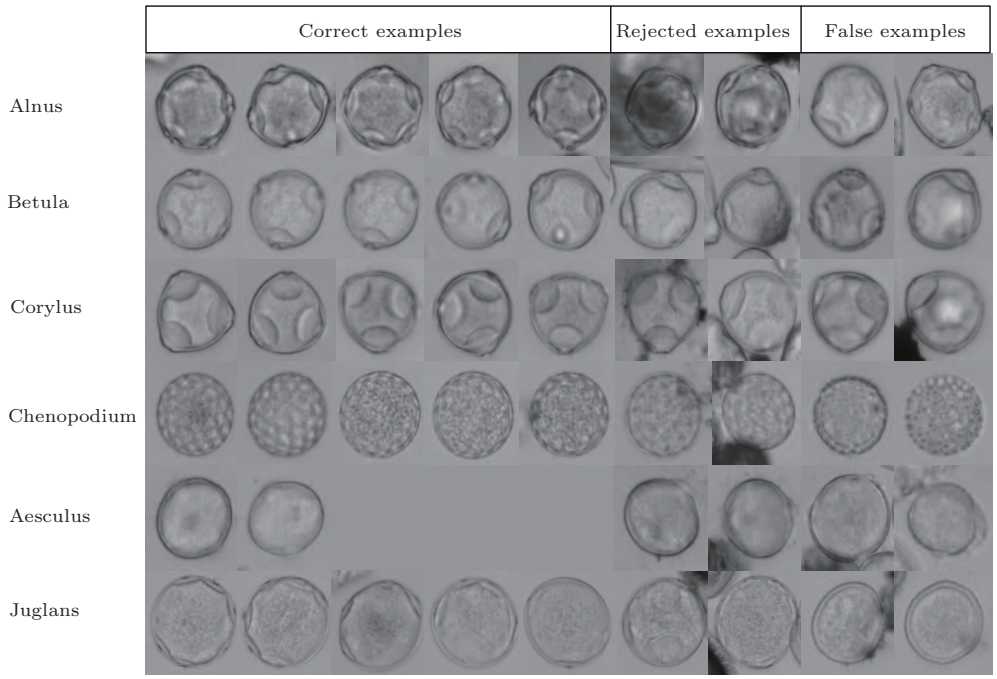


Fig. 5. Top recognition examples of six pollen categories from the Pollenmonitor dataset.

Table 3. Recognition results of six pollen categories from the Pollenmonitor dataset.

Pollen category	CRR/%	RR/%	FRR/%
Alnus	88.2	5.7	6.1
Betula	81.5	7.9	10.6
Corylus	90.8	3.3	5.9
Chenpodium	87.8	6.8	5.4
Aesculus	43.2	26.4	30.4
Juglans	82.6	13.6	3.8

Table 4 presents the comparison of average recognition results based on the different descriptors on the Pollenmonitor dataset. The corresponding recognition performance of average recognition precision versus average recall rate is presented in Fig. 6. It is obvious that the recognition performance of the proposed SGCHD is still superior to that of the other four methods on the low-quality pollen images. The average correct recognition rate can reach 89.2% with the 6.7% rejected rate and 4.1% false recognition rate, which outperforms that of the other descriptors by 9.6% averagely. Meanwhile,

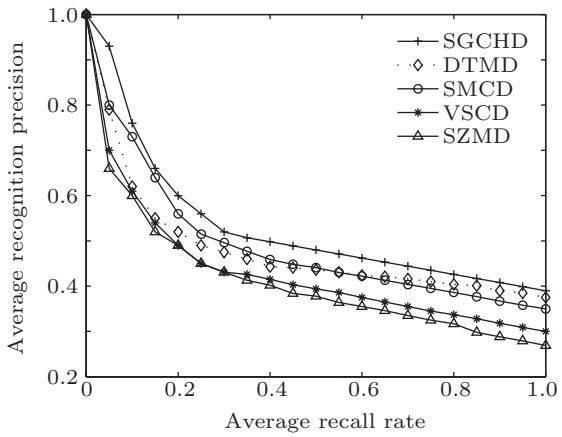


Fig. 6. Average recognition precision versus average recall rate on Pollenmonitor dataset.

compared with the four traditional methods, the feature dimensionality of SGCHD can be reduced by about 90.0% on average and the recognition time can be limited to 6.9 s. Satisfactory results on the Pollenmonitor dataset further validate the good geometric invariance and high compactness of the proposed SGCHD features.

Table 4. Contrast recognition results of different descriptors on the Pollenmonitor dataset.

Descriptors	FN	CRR/%	RR/%	FRR/%	RT/s
SZMD	10892	70.3	16.2	13.5	20.9
DTMD	20671	86.0	8.7	5.3	28.3
SMCD	13620	78.6	12.5	8.9	13.7
VSCD	6280	83.5	9.3	7.2	12.6
SGCHD	2132	89.2	6.7	4.1	6.9

5. Conclusions

This paper presents a new method for 3D pollen particle recognition based on SGCHD. There are two aspects to the advantages of our methods. On one hand, discrete curvature voxels can be used to represent the principal 3D image surface information, which can greatly reduce the high dimensionality and noise disturbance on the surface. On the other hand, the extracted SGCHD features are invariant to different pollen image geometric transformations, such as pose change and spatial rotation. Consequently, the effective feature description ability and geometric invariance make it quite suitable for practical pollen recognition.

Acknowledgments

The authors thank the anonymous reviewers for their valuable comments and helpful suggestions.

References

[1] Bush M B and Weng C Y 2007 *Journal of Biogeography* **34** 377
[2] Xie Y H and Michael O 2010 *Chin. Phys.* **19** 110601
[3] Zhou X L, Chen X R, Yang X D and Gou Q Q 2003 *Chin. Phys.* **12** 1011
[4] Tian H, Cui W R, Wan T and Chen M 2008 "A Computational Approach for Recognition of Electronic Microscope Plant Pollen Images" (CISP 2008), *Proceedings of the* 2008 *International Congress on Image and Signal Processing* Haikou, Hainan, p. 259
[5] Allen G P, Hodgson R M, Marsland S R, Arnold G, Flemmer R C, Flenley J and Fountain D W 2006 "Automatic Recognition of Light-Microscope Pollen Images", *Proceedings of the* 21*st International Conference on Image Vision and Computing*, November 27–29, Great Barrier Island, New Zealand, p. 355
[6] Steven S, Eckart S, Ulrich H, Regula G, Claudio D, Barbara K, Burkhardt H, Olaf R, Wang Q, Albrecht B, Gerd S, Markus E V, Dominik G, Markus F, Wolfgang K, Wilhelm D, Hubert L, Werner M and Gernot B 2006 *Automatic Pollen Recognition: Developments and Perspectives, Nachrichtenblatt des Deutschen Pflanzenschutzdienstes* **58** 309
[7] Li Z, Zhang J S, Yang J and Gong Q H 2006 *Chin. Phys.* **15** 2558
[8] Pierre B, Alian B, Monique T, Regis T, Pablo G H, Jordina B and Carman G 2002 *Image Anal. Stereol.* **20** 527
[9] Fehr J, Ronneberger O, Kurz H and Burkhardt H 2005 "Self-Learning Segmentation and Classification of Cell-Nuclei in 3D Volumetric Data using Voxel-Wise Gray Scale Invariants", *Proceedings of the* 27*th DAGM Symposium* , August 31–September 2, 2005, Vienna, Austria, p. 377
[10] Ronneberger O, Burkhardt H and Schultz E 2002 "General-Purpose Object Recognition in 3D Volume Data Sets using Gray-Scale Invariants-Classification of Airborne Pollen-Grains Recorded with a Confocal Laser Scanning Microscope", *Proceedings of the* 16*th International Conference on Pattern Recognition*, August 11–15, 2002, Quebec, Canada, p. 290
[11] Olaf R, Wang Q and Burkhardt H 2007 *Lecture Notes in Computer Science* **4713** 425
[12] Wang Q, Ronneberger O and Burkhardt H 2009 *IEEE Transactions on Pattern Analysis and Machine Intelligence* **31** 1715
[13] Wong W, Shih F Y and Liu J 2007 *Information Sciences* **177** 1878
[14] Valveny E and Marti E 2003 *Pattern Recognition Letters* **24** 2857
[15] Yang S 2005 *IEEE Transactions on Pattern Analysis and Machine Intelligence* **27** 278
[16] Peng S H, Kim D H, Lee S L and Chung C W 2010 *Information Sciences* **180** 2925
[17] Qin W, Zhang Z H and Liu X H 2011 *Acta Phys. Sin.* **60** 127303 (in Chinese)
[18] Arici T, Dikbas S and Altunbasak Y 2009 *IEEE Transactions on Image Processing* **18** 1921
[19] Yang P F, Wu F M, Teng B T, Liu S and Jiang J Z 2010 *Chin. Phys.* **19** 097104
[20] Ronneberger O 2007 "3D Invariants for Automated Pollen Recognition", Ph. D. Thesis, (Germany: Freiburg University)